Geofísica Internacional (2026) **65-2**: 1- 16

Investigation of Geometrical extent of geologic formation in the Southwestern Sokoto Basin Nigeria: Airborne and Landsat 8 Classification

N.K Olasunkanmi and U.Z Magawata

Abstract

High-resolution airborne geophysical datasets from part of the southwestern Sokoto basin, northwestern Nigeria, were utilized to characterize lithological units and map their geometrical extent. The major lithological features interpreted from Landsat 8 Operational Land Imager (OLI) images and total magnetic intensity data facilitate the identification of variations in minerals and lithological units, including quartz, biotite gneiss, biotite granite, feldspathic sandstone, sandstone, ironstone, granite gneiss, and migmatite. The radiometric ternary map displayed geologic features quite similar to those on the Landsat 8, magnetic, and geological maps of the study area. 3D Euler deconvolution corroborated the SOURCE PARAMETER IMAGING (SPI) for estimated depth to concealed magnetic sources range within ≤200 m, 317.7 m to 500 m, and above 780 m, for shallow to intermediate and deeper depths, respectively. Euler solutions for the structural index (SI) of 0 and 1 revealed a perfect cluster along notable geologic features such as faults, shear zones, and lithological boundaries, mapped using the OLI multispectral band, lateral lithological boundaries, and the vertical geometry of the geologic formation within the southwestern part of the Sokoto basin. The research highlighted the advantages of utilizing airborne and multispectral datasets to achieve a more comprehensive characterization of the lithological units exposed at the surface.

Key words: Geometry of geologic features, Sokoto basin, magnetic source bodies, Multispectral band.

Resumen

Se utilizaron conjuntos de datos de geofísica aérea de alta resolución de una parte de la cuenca suroeste de Sokoto, en el noroeste de Nigeria, para caracterizar las unidades litológicas y mapear su extensión geométrica. Las principales características litológicas interpretadas a partir de las imágenes del Landsat 8 Operational Land Imager (OLI) y de los datos de la intensidad magnética total, facilitaron la identificación de las variaciones en las unidades minerales y litológicas, tales como el cuarzo, gneis de biotita, granito de biotita, arenisca feldespática, arenisca, hierro, gneis granítico y migmatita. El mapa ternario radiométrico mostró características geológicas bastante similares a las del Landsat 8, el mapa magnético y el mapa geológico del área de estudio. La deconvolución de Euler en 3D corroboró la imagen de parámetros de fuente (SPI) para la profundidad estimada de las fuentes magnéticas ocultas, que oscila en ≤ 200 m, de 317,7 m a 500 m y por encima de 780 m, para profundidades superficiales, intermedias y profundas, respectivamente. La solución de Euler con índices estructurales SI de 0 y 1 reveló un agrupamiento perfecto a lo largo de notables características geológicas tales como: fallas, zonas de cizalla y límites litológicos mapeadas con la banda multiespectral OLI, límites litológicos laterales y la geometría vertical de la formación geológica dentro de la parte suroeste de la cuenca de Sokoto. La investigación destacó las ventajas de utilizar datos de geofísica aérea y multiespectrales para lograr una caracterización más completa de las unidades litológicas expuestas en la superficie."

Palabras clave: Geometría de características geológicas, Cuenca de Sokoto, cuerpos fuente magnéticos, banda multiespectral.

Received: November 4, 2024; Accepted: December 30, 2025; Published on-line: April 1, 2026.

Editorial responsibility: Dr. Óscar C. Valdiviezo Mijangos

* Corresponding author: U. Z Magawata, uzayyanu@yahoo.com
[1] Kwara State University, Physics and Materials Science Department Malete Kwara State Nigeria.
[2] Abdullahi Fodio University of Science and Technology, Physics Department, Aliero Kebbi State Nigeria.

Kolawole Nurrudeen Olasunkanmi, Usman Zayyanu Magawata

https://doi.org/10.22201/igeof.2954436xe.2026.65.2.1836

1. Introduction

The Nigerian sedimentary basins, comprising sediments deposited from the Cretaceous to the Tertiary, encompass the Chad Basin, the Lower, Middle, and Upper Benue Trough, the Niger Delta, the Anambra Basin, the Dahomey Basin, the Mid-Niger (Bida-Nupe) Basin, and the Sokoto Basin (Kogbe, 1979). The Sokoto (Iullemmeden) basin is a circular intracratonic basin in the south–central Saharan African region, covering ~700,000 km^2. It stretches across parts of Mali, Benin, and the Niger Republic, and northwestern Nigeria (Obaje, 2009). The basin sediment accumulated over three major episodes and was affected by several marine transgressions (Kogbe, 1979). The first is the Illo and Gundumi formations, which were deposited unconformably on the Precambrian basement complex during the continental period. This formation comprises the grits and clays from West Africa's continental intercalary. The Maastrichtian transgression began in the second and continued into the Paleocene (Adeleye, 1979), resulting in the Rima Group (Maastrichtian) and the Sokoto Group (Paleocene). The third phase began in the Eocene with the regression of the sea. The overlying Gwandu formation forms the Post-Paleocene continental terminal (Kogbe, 1981). These continental conditions, until the present day, prevail. Some segments of the Sokoto basin were characterized by outcropping Precambrian crystalline rocks from the east and south, including amphibolite gneisses, phyllites, granite, and quartzite (Kogbe, 1979).

The basement complex components include the Pan-African granitoid, basic dykes, undeformed acid, migmatite gneiss, and schist belts (Fitches *et al.*, 1985). The area falls within the southwestern Sokoto basin, bounded by longitude of 3° 30′’00’ to 5° 30′’00’ and latitudes 10° 00′’00’ to 12° 00′’ 00’ (Figure 1) and cut across one of the auriferous Neoproterozoic schist belts named Zuru Schist Belt (Wright, 1985; Garba, 2000, 2003). It contains a supracrustal rock that is infolded into the migmatite-gneiss basement complex. The Sokoto basin lithology’s characteristics are available in the literature (Kogbe, 1979; Wright, 1985; Offodile, 2002; Obaje, 2009, 2013; Nwajide, 2013; Emujakporue *et al.*, 2018), where the studies are based on extrapolation of the notable geologic formations and some geophysical and/or geochemical approaches in some selected locations (Ademila *et al.*, 2018; Okon *et al.*, 2020; Olasunkanmi *et al.*, 2023; Fagbohun *et al.*, 2021; Aisabokhae & Osazuwa, 2021; Ekwok *et al.*, 2021; Augie *et al.*, 2022; Magawata *et al.*, 2024), and also on Landsat 8 multispectral data used to identify different lithological assembly (Sabin, 1987; Deroin, 2019; Akinsunmade *et al.*, 2020; Olatunji, 2022; Ghrefat *et al.*, 2021; Olasunkanmi *et al.*, 2022). However, there are information gaps about the actual or inferred geometry (longitudinal and vertical extent) of the study area. The application of airborne magnetic survey, singularly or integrated with radiometric and/or Landsat 8 data, has proven practical techniques in identifying regional surficial rock boundary formation (Sabin, 1997; Allou & Bonin, 2015; Waswa *et al.*, 2015; Akingboye *et al.*, 2018; Ekwork *et al.*, 2021; TakodjouWambo *et al.*, 2020; Traore *et al.*, 2020; Magawata *et al.*, 2025). This study primarily aims to utilize a high-resolution airborne dataset and Landsat 8 multispectral images to characterize the lithological boundaries and geometry of the area. Moreover, the methods employed in this study have proven successful in distinguishing lithotypes and improving geological mapping.

2. Data compilation and pre-processing

Integrated approaches involving aeromagnetic, radiometric, and Landsat 8 multispectral datasets are used to characterize lithological boundaries and geometry (lateral and vertical extent) of basins (Evans, 1988; Ali & Pour, 2014; Ekwork, 2021; Farah *et al.*, 2021; Okon *et al.*, 2020; Ghrefat *et al.*, 2021), data completion and subsequently process by which the methodology and results were obtained are shown in the flowchart (Figure 2).

2.1 Digital elevation model

The digital topography variations of the area, which are displayed as images and indicate the elevation variations in meters, were generated from the DIGITAL ELEVATION MODEL (DEM). The data are from the National Aeronautics and Space Administration’s (NASA) Shuttle Radar Topography Mission (SRTM). The highest elevation ranges from 280 to 332 m, occupies the eastern part of the study area, and corresponds to metamorphic rocks or volcanic igneous activity that have exposed or raised the surface. In comparison, the western zone has low elevations ranging from 174 to 232 m above sea level. The DEM inferences match the estimated amplitude of the analytical signal (ASA) map for both shallow and deeper magnetic sources.

2.2. Landsat 8 images

High-resolution remotely sensed Landsat 8 OLI images of the study area, part of the Sokoto Basin, Nigeria, were acquired from the United States Geological Survey (USGS) archive (USGS, 2021). It is level L1, collection C2, covering the entire study area with a four-scene image mosaic (190, 052; 12/01/2021; 190, 053; 02/01/2021; 191, 052; 28/04/2021; and 191, 053; 15/02/2021). Atmospheric correction was applied to minimize noise in the data. The data were georeferenced using Universal Transverse

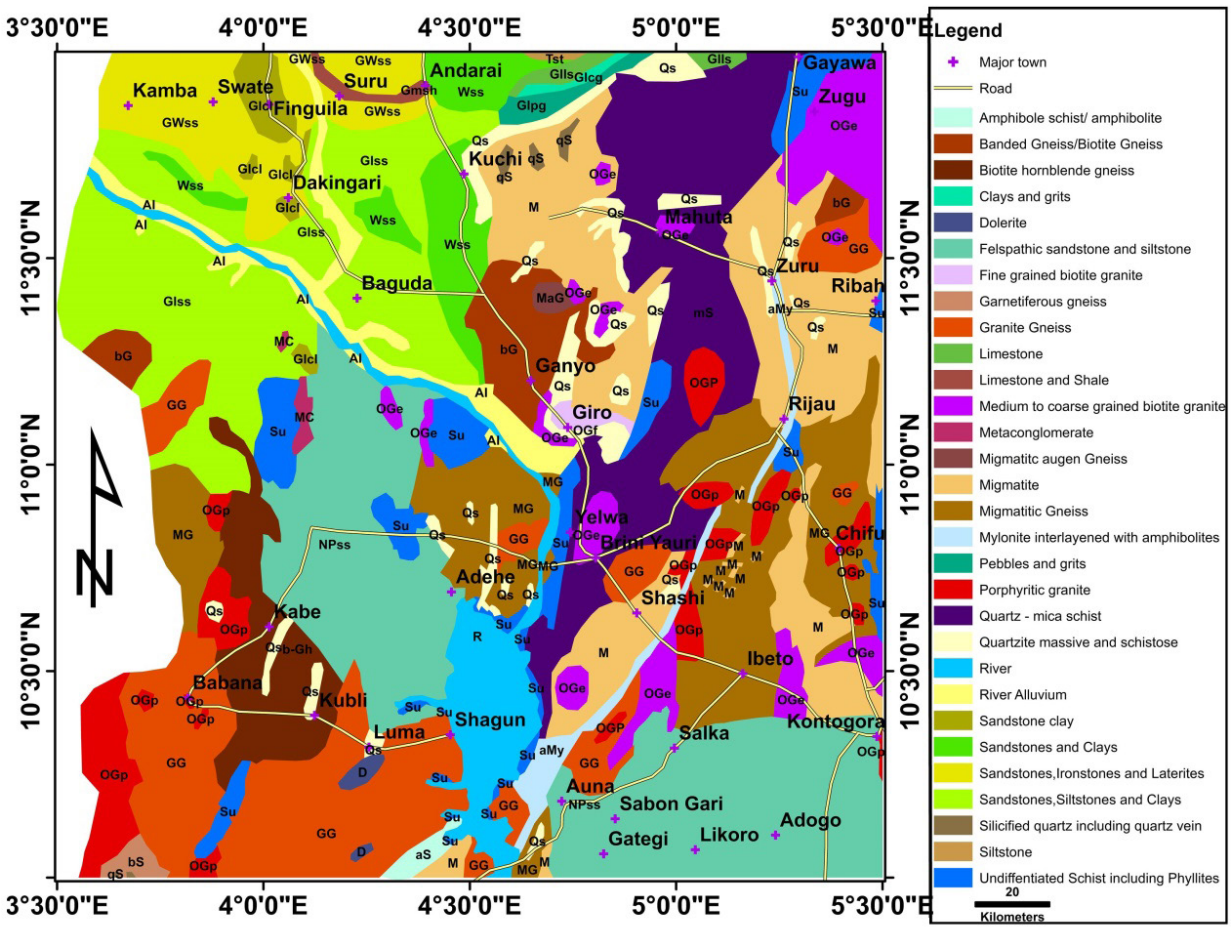


Figure 1. Geological map of the study area part of Sokoto basin, showing the representative rocks distribution of the basin after (NGSA, 2009).

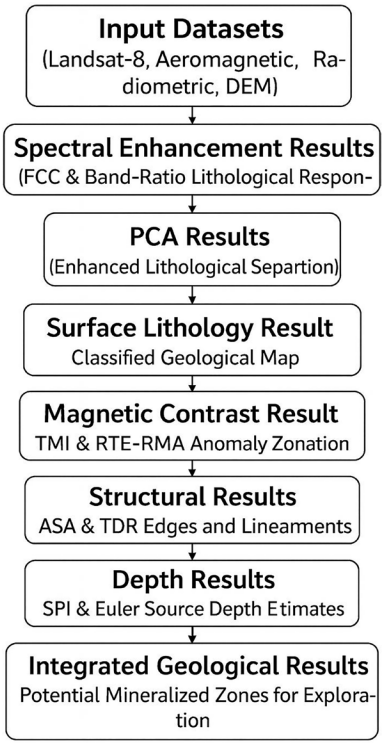


Figure 2. Flow chart showing how the results were obtain.

mercometer (UTM) 32N, WGS 84. The high-resolution images were selected based on their spectral and spatial characteristics, which enable effective lithological mapping of the study area. Using the color-composite method, the multispectral bands are displayed in red, green, and blue (RGB).To produce RGB color images (Figure 3a), selective bands within the Visible and infrared regions of the electromagnetic spectrum were combined (Evans, 1988). Based on the spectral dominance of the lithology's assembly depicted in Figures 3b–g. Many forms of Band ratio (BR) are frequently used to establish Landsat 8 data according to their application, such as lithology mapping, hydrothermal variation/and or alteration, and enhance the color contrast that could differentiate rock types, and to reduce the dimensionality in Landsat 8 data (Poor & Hashim, 2015). The principal component analysis (PCA) is based on multispectral remote sensing data, as depicted in Figure 3, based on the output bands (1, 2, 3, 4, 5, 6) of Landsat 8 OLI, which were engaged in accordance with (Aisabokhae & Osazuwa, 2022; Traore *et al.*, 2020).

High-resolution remotely sensed Landsat 8 OLI images of the study area, part of the Sokoto Basin, Nigeria, were acquired from the United States Geological Survey (USGS) archive (USGS, 2021). It is level L1, collection C2, covering the entire study area with a four-scene image mosaic (190, 052; 12/01/2021; 190, 053; 02/01/2021; 191, 052; 28/04/2021; and 191, 053; 15/02/2021). Atmospheric correction was applied to minimize noise in the data. The data were georeferenced using Universal Transverse mercometer (UTM) 32N, WGS 84. The high-resolution images were selected based on their spectral and spatial characteristics, which enable effective lithological mapping of the study area. Using the color-composite method, the multispectral bands are displayed in red, green, and blue (RGB).To produce RGB color images (Figure 3a), selective bands within the Visible and infrared regions of the electromagnetic spectrum were combined (Evans, 1988). Based on the spectral dominance of the lithology's assembly depicted in Figures 3b–g. Many forms of Band ratio (BR) are frequently used to establish Landsat 8 data according to their application, such as lithology mapping, hydrothermal variation/and or alteration, and enhance the color contrast that could differentiate rock types, and to reduce the dimensionality in Landsat 8 data (Poor & Hashim, 2015). The principal component analysis (PCA) is based on multispectral remote sensing data, as depicted in Figure 3, based on the output bands (1, 2, 3, 4, 5, 6) of Landsat 8 OLI, which were engaged in accordance with (Aisabokhae & Osazuwa, 2021; Traore *et al.*, 2020).

2.3 High-resolution airborne magnetic

Sixteen sheets (gridded on 55 km × 55 km per data sheet) of aeromagnetic dataset for this study were acquired from the Nigeria Geological Survey Agency (NGSA). The survey was carried out by Fugro Aero Services Ltd. between 2004 and 2009 for mineral resources development in Nigeria (NGSA, 2009), using Scintrex Cesium vapor magnetometers installed on a Cessna Caravan fixed-wing aircraft. The newly acquired high-resolution data were recorded along 500-m line spacing in the NW-SE direction, 80 m train clearances, and 2000 m tie line spacing in the NE-SW direction. TOTAL MAGNETIC INTENSITY (TMI) maps were generated from the dataset (Figure 5a). Additionally, Standard corrections, including interpolation, diurnal variation removal, height correction, and differential polynomial fitting, were applied. The international geomagnetic reference field was removed from the total field, and the resultant RESIDUAL MAGNETIC INTENSITY (RMI) was enhanced by employing REDUCTION TO THE EQUATOR–RESIDUAL MAGNETIC ANOMALY (TE–RMA) (Figure 5b) at inclination and declination angles I= 3.021 and D= −0.245. The RTE was employed to remove the inclination effect in low-latitude regions. The RTE-RMA enhances the magnetic anomalies contrast associated with lithologic sequence (Rajagopalan, 2003; Ndousa-Mberga *et al.*, 2012) and contributes to making the anomalies symmetrical to their sources and specifying their contours (Raoufou *et al.*, 2016; Akinlalu *et al.*, 2018; Akinsunmade *et al.*, 2020; Olasunkanmi *et al.*, 2020).

The TMI is subjected to Analytic Signal, and the resulting analytical signal amplitude 'ASA' (Figure 6a) is acquired from three orthogonal derivatives in the *x* and *y* direction and the vertical gradient (Roest *et al.*, 1992; Macleod *et al.*, 1993). The amplitude signal is a combination of the total directional gradients of the magnetic field (A), which estimates the position of magnetic contacts at shallow levels (Nabighian, 1972; Akinlalu *et al.*, 2018; Okpoli & Akingboye, 2019; Saleh *et al.*, 2020; Olasunkanmi *et al.*, 2020). The TILT DERIVATIVES (TDR) (Figure 6c) method was employed to enhance weak magnetic anomalies and directly realign them with their sources. The weak anomalies are overshadowed by stronger structures (Verduzco *et al.*, 2004; Salim *et al.*, 2007). The VERTICAL DERIVATIVE (VDR) is a vertical derivative in the Z-direction, and horizontal gradient magnitudes (HGM) are derivatives in the X- and Y-direction. The SPI method was used to evaluate the depth of the magnetic basement (Thurston & Smith, 1997). The parameters that make a body, including susceptibility contrast, depth, and dip, are computed from the complex ANALYTICAL SIGNAL AMPLITUDE (ASA), respectively (Nabighian, 1972). The SPI technique is independent of a user-selected window, unlike other methods, such as spectral analysis, that depend on it. The 3D Euler deconvolution is an automated potential field interpretation technique used to estimate the location and depth

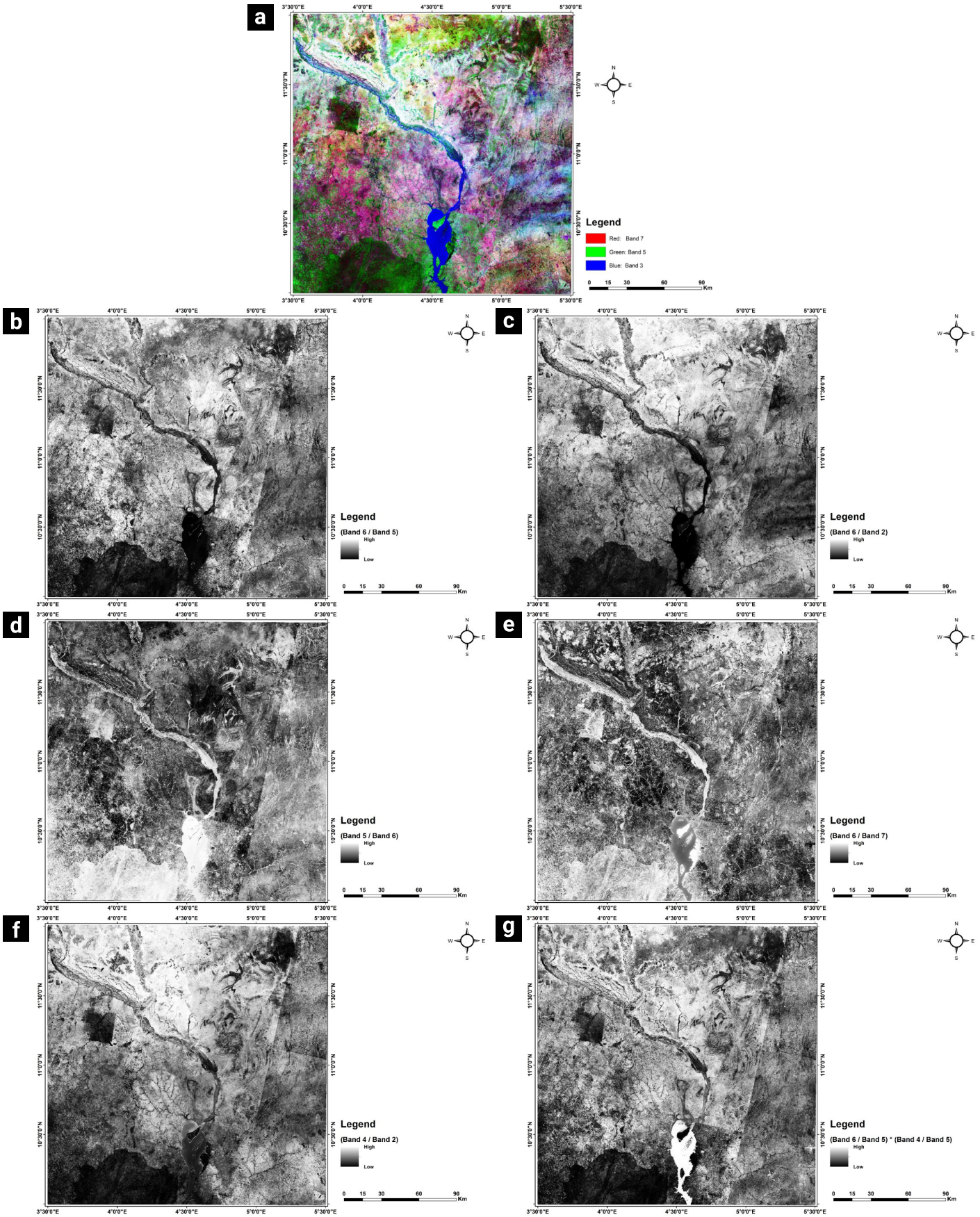


Figure 3. False color composite maps within the visible and infrared regions (a) RGB band and Gray scale Band ratio (b) 5/6 (c) 6/2 (d) 6/5 (e) 6/7 (f) 4/2, and (g) 6/5* 4/5 showing various lateral geologic features of the area.

of subsurface magnetic sources by exploiting the relationship between a measured field and its spatial gradients. It is based on Euler's homogeneity equation, which links the magnetic field, its derivatives in the *x*, *y*, and *z* directions, and a structural index (SI) that represents the expected source geometry (e.g., contact, dyke, sill, or sphere).

In this study, 3D Euler deconvolution was applied to the reduced to equator (RTE) magnetic data using appropriate structural indices to solve for source positions and depths. The resulting depth solutions were spatially clustered and filtered to remove outliers. These solutions were then compared with SPI depth estimates, magnetic anomaly boundaries, and mapped lineaments. The good spatial coincidence between Euler depth clusters, structural trends, and zones of magnetic contrast corroborated the interpreted structures and depth estimates, thereby increasing confidence in the delineation of subsurface geological features and potential mineralized zones. However, the 3D Euler assumes a simple geologic model related to different structural indices (Reid *et al.*, 1990; Roest *et al.*, 1992). The STRUCTURAL INDICES SI=0 or 0.5 for contact in three dimensions 3D, SI=1 depicts intrusive bodies in TWO-DIMENSIONAL 2D (Silk and Dyke), and SI=2 for horizontal cylinder or vertical bodies (pipes) (Akinlalu *et al.*, 2018; Olasunkanmi *et al.*, 2020). The Sixteen sheets (16) of the aero-radiometric dataset are acquired from the NGSA and used for the southwestern Sokoto basin. The data were acquired by Fugro Aero Services for NGSA using individual Advanced Digital high-resolution Gamma-ray spectrometers (ADS, model Rs-500) mounted on the aircraft wing, with an average terrain clearance of 80 m. Airborne Radiometric surveys depend on a measurement of gamma rays from the natural decay of potassium (K), thorium (eTh), and uranium (eU) in shallow rocks/soil (Dentith & Mudge, 2014). The enhancement techniques that involve color composites on MAGMAP.omn tools in Oasis Montaj 8.4.1 were applied to obtain concentrations of potassium (%), thorium (ppm), and uranium (ppm) (Figures 9a, 9b, and 9c). In comparison, the channel ratio (eTh/K) (Figure 10a) and ternary imageries (Figure 10 b) are engaged in obtaining the maps to correlate with the trend and pattern of the geological units for lithological/or geochemical mapping (Korhonen, 2005; Airo & Mertanen, 2008; Ranjbar *et al.*, 2011).

3. Result and Discussion

3.1 Multispectral surface geological sequence

The spectral signatures of the optimal false color composite in the RGB image "bands 7, 5, and 3" (Figure 3a) are visually inspected and compared with the extrapolated lithological units. The FCC-RGB image depicts the dominant lithologic units, with pink to red colors corresponding to metamorphic rocks such as migmatite gneiss, amphibolite, porphyritic granite, and mica-biotite within the east–south region. While the green color corresponds to the older granitoids, viz., granite gneiss, quartz, mica, and schistose rocks that occurred in the southwestern and northern regions, the deep-light blue color reveals the central water body (a tributary to Kainji Lake) and alluvium. Other band-ratio images further enhanced the FCC-RGB to reveal the obscured lithologic units, viz., the sedimentary, metasedimentary, metamorphic, and older granitoid, in concordance with the tone of FCC-RGB.

The band ratio image 6/5 depicts the sedimentary and some metasedimentary rocks, such as sandstone, limestone, siltstone, clays, and feldspathic sandstone and biotite gneiss rock majorly in a bright tone, granite gneiss, and water body in a dark tone, and metamorphic rocks such as migmatite gneiss, medium to coarse-grained biotite in gray tone (Figure 3b). In-band ratio 6/2 corresponds to sedimentary rocks composed of sandstone, i.e., subarkose (feldspathic arenite), laterite, ironstone, and limestone, displayed in bright tones, with dark tones observed within the sedimentary strata, which are suspected to be metamorphic or older granitoid rock. In contrast, metamorphic rocks identified as migmatite and granite gneiss show in gray tones, and some granitoid rocks contain granite gneiss; however, dark tones were observed in waterways, as seen in Figure 3c. The band ratio, 5/6, displayed rocks of older granitoid, typically granite gneiss, porphyritic granite, and waterway in a bright tone. Metamorphic and metasedimentary rocks delineate migmatite gneiss, sandstone, and amphibolite in gray tone, and dark tone delineates banded gneiss (Figure 3d). The image 6/7 band ratio displayed metamorphic and gneiss rocks, typically the granite gneiss, phyllite, and quartz mica schist rocks, in a bright tone.

Igneous rocks show coarse-grained biotite and granite gneiss in gray, and metasedimentary rocks, mainly sandstone and ironstone, in dark tones (Figure 3e). The band ratio (4/2) shows the sedimentary rocks, such as siltstone, clay, and laterite, in bright tones. The gray tone suggests metamorphic rocks such as quartz mica, granite, and migmatite gneiss, and waterways in dark tones (Figure 3f), in accordance with (Ahmed, 2020; Aisabokhae & Osazuwa, 2021; Amara *et al.*, 2019). The band ratio 6/5* 4/5 of the grayscale image depicts the sedimentary rock in a bright tone. In contrast, a rock composed of older granite revealed granite, migmatite, and porphyritic granite rocks displayed in gray and undifferentiated schist, including phyllites in a dark tone, as seen in Figure 3g. The BR provides better discrimination of some rocks in the study area, since remote sensing data captures surface information related to rock exposure.

3.1.1 Principal Component Analysis 'PCA'

PCA, on the other hand, tends to give better results than BR. The PCA result revealed the highest percentage of data variance traced in (PC1), while (PC6) experienced low variance due to the noise interfering within the exact spectral bands (Figure 4a). The PCA results show eigenvectors for different bands, with the input bands shown in Table 1. The rocks were differentiated into bands 3, 2, and 1 in Red, Green, and Blue (RGB) color, respectively. The PCA delineates sedimentary rocks (pink) that majorly occupy the northwestern region, and metasedimentary rocks (yellow to light purple) of band three occur in a sporadic pattern within the study area.

In contrast, metamorphic rocks in the greenish color of band 2 trended the eastern part of the study area, and older granitoid in the blue to purple color of band 1 dominated the extreme southern

Table 1. Eigenvector loading for PCA of Landsat 8 data (bands 2–7).

Eigenvectors	Band 2	Band 3	Band 4	Band 5	Band 6	Band 7	Eigenvalues 100%
Band 2	0.136595	0.252239	0.537735	0.192033	0.459991	0.616514	85.72
Band 3	0.320499	0.512333	0.535542	−0.18579	−0.40121	−0.39052	7.97
Band 4	0.131894	0.016435	−0.15144	−0.86201	−0.11524	0.450621	3.86
Band 5	0.618053	0.446456	−0.59487	0.194467	0.163474	0.016714	1.57
Band 6	−0.05045	0.052198	−0.08438	0.378557	−0.76174	0.513858	0.75
Band 7	−0.69043	0.686711	−0.20029	−0.0665	0.084747	0.004188	0.13

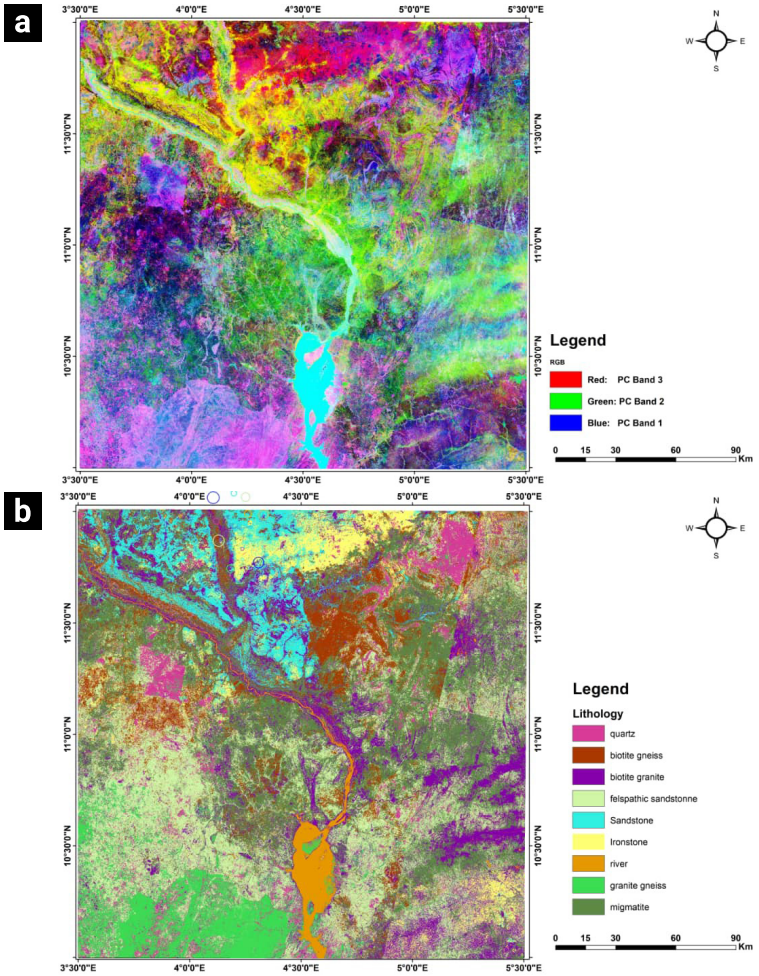


Figure 4. (a) Color composite of the first three PCA, Eigen channels red (PC3), green (PC2), blue (PC1) as RGB, (b) lithological map of the area.

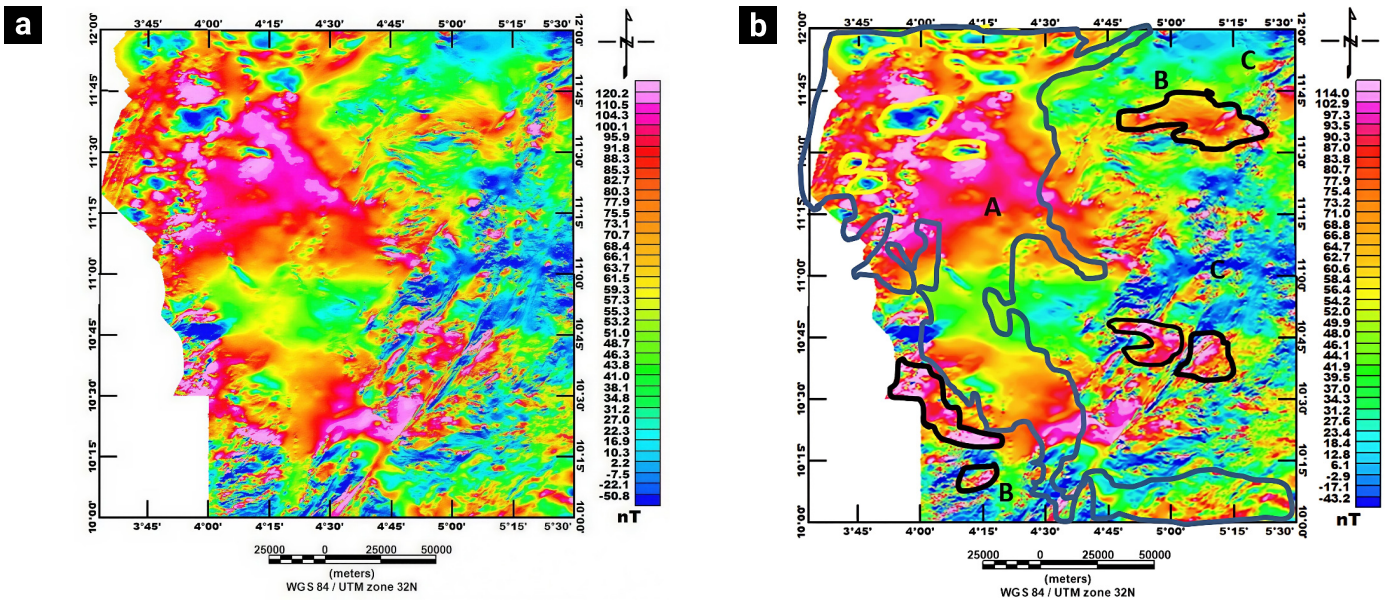


Figure 5. (a) Total magnetic intensity (TMI) map, (b) Reduced to equator-residual magnetic anomaly map, showing the magnetic contrast of southwestern Sokoto basin.

part. Subsequently, band 6 contributed more than the other bands, with PC1 accounting for 85.72% of the total variance. Based on the geological information, PC1, PC2, and PC4 were selected. The visual interpretation indicates that the information obtained was consistent with the area's geological information. Band-ratio analyses are used to obtain image classification using a likelihood classifier. The obtained image is fairly accurate in representing the lithological map (Figure 4b). Subsequently, the lithological assemblies are well identified and appear in eight lithotypes of different contour rocks: (1) quartz, (2) biotite gneiss, (3) biotite granite, (4) felspathic sandstone, (5) sandstone, (6) iron stone, (7) granite gneiss, and (8) migmatite.

3.2 Magnetic contrast mapping

The shaded relief TMI map (Figure 5a) is characterized by positive magnetic intensity ranging from 2.2nT to 120.2nT and negative values ranging from −50.8nT to −7.2nT, which has the same trend of magnetic intensity contrast but enhanced variation in value on the RTE–RMA map, ranging from 6.1nT to 114.0nT and negative values ranging from −2.9nT to 43.2nT. The magnetic variation differentiates the magnetic contrast into high, intermediate, and low levels, depicted in RGB colors. The RTE–RMA map delineates three zones, which were categorized based on the difference in the intensity of the magnetic response and varying color of the TMI and RTE–RMA maps, viz; magnetic highs “A” (Red), intermediate “B” (Green), and magnetic lows: “C” (Blue) (Figure 5b). The conspicuous maximum magnetic anomalies “A” range from 52.0nT to 114.0nT and correspond to the sedimentary rocks established by FCC-RGB in the northwestern zone and some portions in the southwestern part. The east–west trending intermediate magnetic amplitude “B” range of 23.4nT to 49.9nT matches weak magnetized felsic rocks (metasediments) crosscutting the country rocks in the eastern and western regions. The predominant low magnetic anomalies “C” within −43.2nT to 18.4nT are attributable to the metamorphic rocks (older granitoid).

However, the RTE–RMA map produces relatively low magnetic anomaly responses within the inferred sedimentary domain depicted in an irregular yellow shape. In comparison, substantial positive magnetic contrast was identified in the metamorphic zone, depicted as a black irregular shape. It may correspond to unidentified lithotypes present in the available geological map of Nigeria produced by the Geological Survey Agency (NGSA, 2009). The blue polygon marks the boundary of the sedimentary basin. Also, high magnetic anomalies may occur in sedimentary terrains when the basement rocks (gneiss, migmatite, and amphibolite) may lie at shallow depths, especially where the Sokoto Basin has a thin sedimentary cover, such as the Gwandu formation, part of the study area, allowing strong basement magnetic signals to penetrate through the sediments (Figure 5b). Also, some sedimentary units may contain magnetic minerals that enhance intensity despite sediments being naturally weakly magnetic. Minerals such as magnetite, hematite, goethite, and ironstone can significantly amplify magnetic responses. In the northwestern part of the study area, the presence of ironstone, ferruginous sandstone, and Fe-rich laterites likely contributes to the observed magnetic highs. The most magnetic lithologies within or beneath the Sokoto Basin include both surface and subsurface units. Surface units such as ironstone in the Gwandu

and Illo Formations produce strong magnetic signatures due to high hematite, limonite, and magnetite contents and commonly appear as red/yellow zones (Figure 5b). Ferruginous sandstone has moderate susceptibility, while laterite enriched with magnetite and maghemite creates localized highs. Subsurface basement rocks such as gneiss, migmatite, amphibolite, and granites containing magnetite generate broad regional magnetic anomalies detectable in aeromagnetic surveys.

3.2.1 Litho-magnetic edge detection and source depth

The maximum amplitude of the analytic signal ASA noticeably revealed the edges of the established metamorphic rocks with values above 0.20nT/m (Figure 6a) trending Southeast and Southwest and corresponding to the low magnetic anomalies and deeper magnetic source depth inferable from high DEM (above 333 m) of the area (Figure 6b). The low amplitude (below 0.01 nT/m) indicates sedimentary rocks trending northwest, corresponding to the high magnetic anomalies and shallow sources, inferred from a low elevation range (≤174 m). The transition zones between sedimentary and basement rock formations, mapped with amplitude of 0.02nT/m, correspond to metasedimentary rocks, major water bodies, and alluvial deposits. The tilt derivative TDR map (Figure 6c) shows linear magnetic patterns with a maximum gradient above 1.30nT/m, while the intermediate gradient is within 0.04–0.19nT/m, and the low gradient is

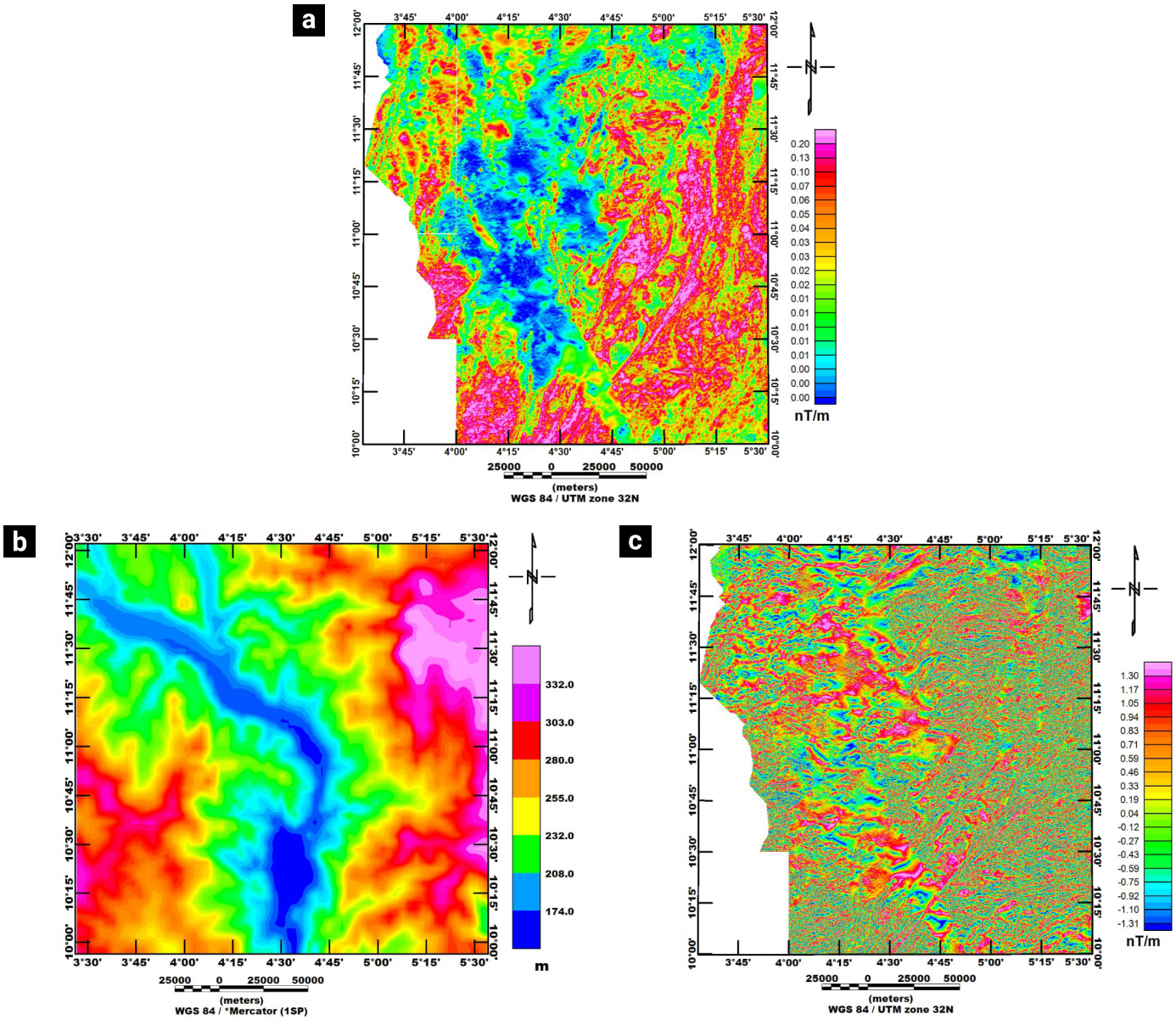


Figure 6. (a) Analytical signal map, (b) Digital elevation model map and inferred rock boundaries (c) Tilt derivative map of the study area.

below −0.12nT/m, corresponding to the deeper magnetic source depth (within the sedimentary), transition zones or rock boundaries. High magnetic anomalies may occur in sedimentary terrains when the basement rocks (gneiss, migmatite, and amphibolite) may lie at shallow depths, especially where the Sokoto Basin has a thin sedimentary cover such as Gwandu formation part of the study area, allowing strong basement magnetic signals to penetrate through the sediments. Also, some sedimentary units may contain magnetic minerals that enhance intensity despite sediments being naturally weakly magnetic. Minerals such as magnetite, hematite, goethite, and ironstone can significantly amplify magnetic responses. In the northwestern part of the study area, the presence of ironstone, ferruginous sandstone, and Fe-rich laterites likely contributes to the observed magnetic highs. The most magnetic lithologies within or beneath the Sokoto Basin include both surface and subsurface units. Surface units such as ironstone (abundant in the Gwandu and Illo Formations) produce strong magnetic signatures due to high hematite, limonite, and magnetite contents and commonly appear as red/yellow zones (Figure 6a). The metasediments, shear zone, and alluvium or water body) and shallow magnetic source depth, respectively. However, the spatial relationships among airborne datasets (Landsat 8, aero-radiometric, and aeromagnetic) provided a robust basis for lithological discrimination (Aisabokhae & Osazuwa, 2021; Ghrefat *et al.*, 2021; Olasunkanmi *et al.*, 2023).

The source parameter imaging (SPI) method estimates magnetic source depths through extended complex analytic signals. The remnant magnetization, magnetic inclination, declination, dip, and strike do not influence the estimation of the depths. The accuracy of SPI is about +/- 20 % in tests on real data sets with drill hole control (Li & Oldenburg, 1996; Thurston & Smith, 1997), and the level of accuracy is similar to that of Euler deconvolution (Li, & Oldenburg, 1996). The SPI map (Figure 7), derived from the RTE map (Figure 5b) shows depth variations range from 85 to 754 m (Emujakporue *et al.*, 2018). The depth range of 85–103.4 m shows a region of shallow-lying magnetic bodies in correspondence with high elevation (above 337 M) within the NE and SW of the area, while thick sedimentary or deep-lying magnetic source depth ranged from 465.2 m to 754 m at a low elevation range below 174 m (Figure 6b).

The corresponding Euler solutions of structural indices SI= 0.5 delineates the magnetic source edges with clusters around notable anomaly of contact between two rock units or very close to critical geological structures such as: faults, fractures, shear zones, lithological boundaries, or folds and established lithology from the ASA and structural trend of TDR at a shallow depth of <166.7 m, which extends to >500 m for the sedimentary thickness (Figure 8a).

The corresponding SI=1, 1.5 depict the contact and edge of intrusive bodies at shallow depth in 2D (Silk & Dyke) at <260 m (Figures 8b and 8c), while for SI=2, the solution depicts the vertical penetrative horizontal cylinder or vertical bodies (pipes)

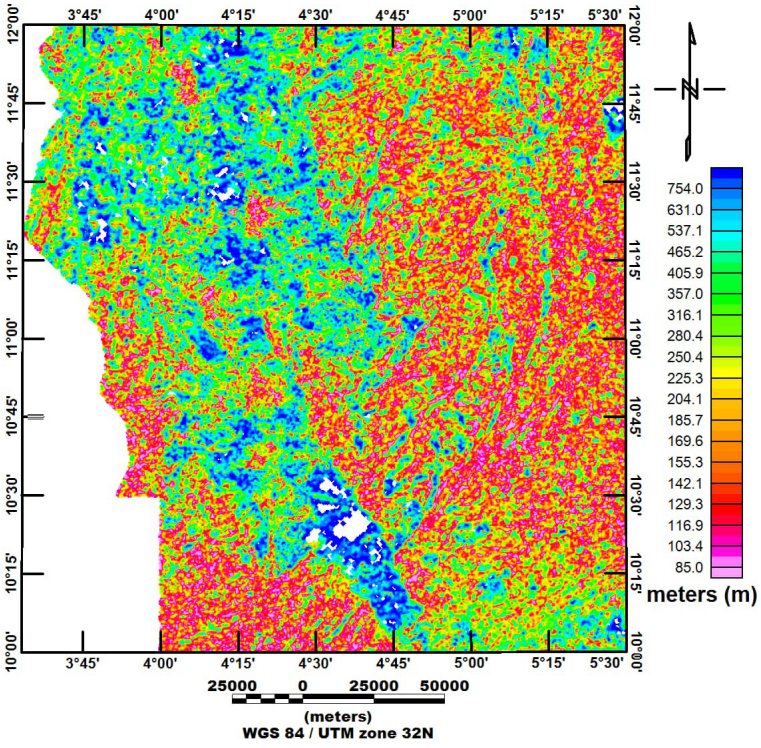


Figure 7. Color-shaded source parameter imaging depth estimate map.

at a depth >959 m (Figure 8d). The corresponding thickness of the basin is above 764.8m, and the delineated structures and their trends coincide with those of SPI (Figure 7). However, the delineated structural features (fractures/faults) trend predominantly in the NE-SW direction, suggesting that the potential mineralization deposit in the area is structurally controlled.

3.3 Radiometric concentration

3.3.1 K/Th/U concentration

The potassium concentration data clearly show that the sedimentary units within the study area contain very low K values (0.09–0.70 %), indicating a general absence of potassium-bearing minerals such as K feldspar. The corresponding value obtained agrees with published descriptions of Sokoto Basin sandstones as feldspar-poor litharenites rather than arkoses. It therefore supports the interpretation that high K sedimentary rocks are not widespread in the area. In contrast, the high K concentrations (2.38–3.17 %) correlate precisely with felsic basement rocks rich in quartz, feldspar, and muscovite, while intermediate K values (0.82–1.90 %) match metasedimentary and mixed schist formations. The close correspondence between the K map and the geological map confirms that the radiometric potassium signal reliably differentiates sedimentary, metasedimentary, and felsic lithologies (Figure 9a). The K-concentration perfectly correlates

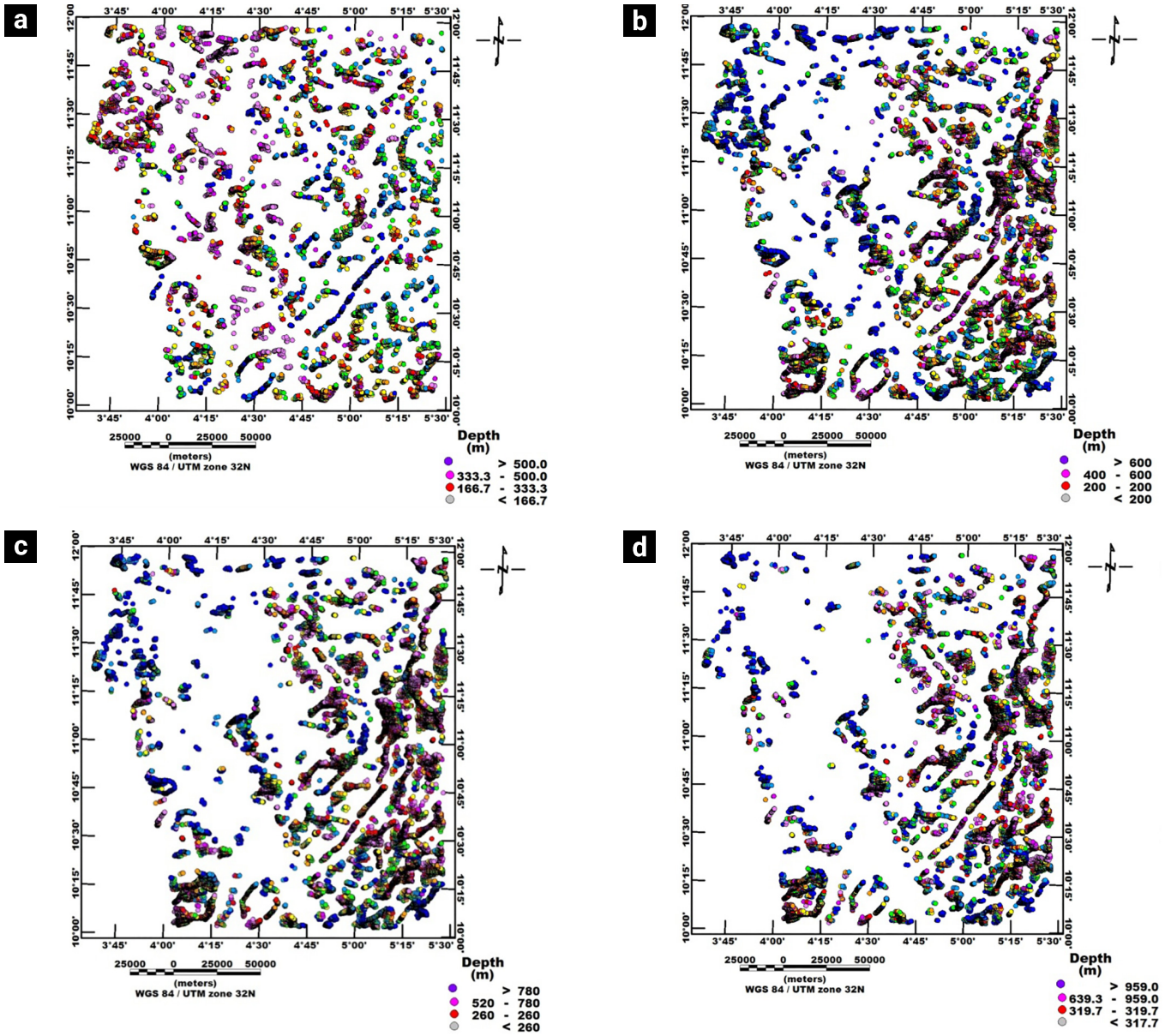


Figure 8. Euler deconvolution maps with Structural Index (a) SI=0.5, (b) SI=1, (c) SI=1.5 (d) SI=2 showing clusters around notable geologic features and prominent NE-SW deformational trend.

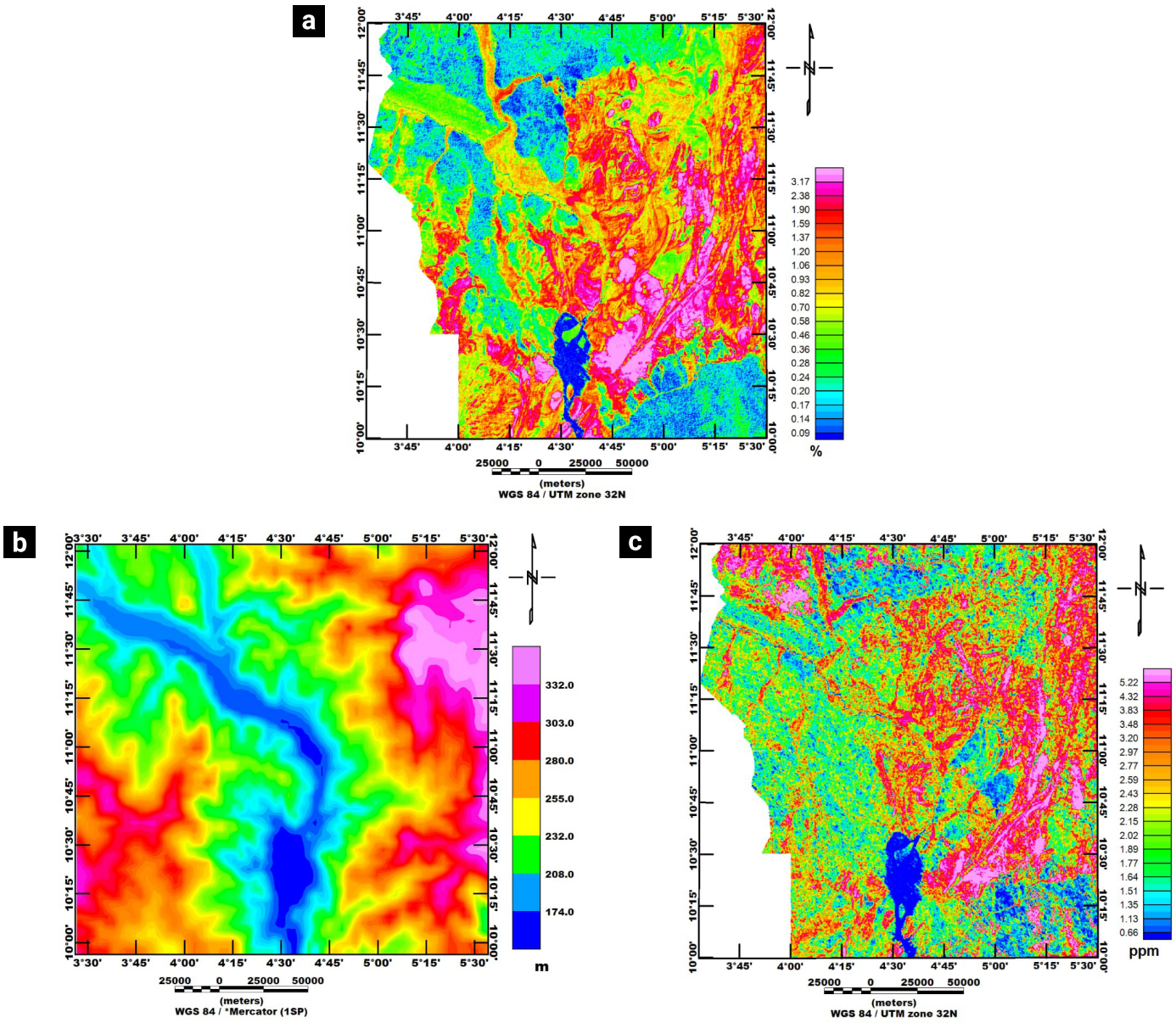


Figure 9. (a) Potassium map (K), (b) Thorium Map (eTh) and,(c) Uranium (eU) map of the area.

with the variation in the amplitude of the ASA (Akinsunmade *et al.*, 2020; Aisabokhae & Osazuwa, 2021). Equivalent thorium (eTh) is an inactive and immobile radioelement; its high concentration within 16.50 ppm –19.85 ppm corroborates the predominant felsic rocks in the eastern region and is associated with intense weathering of mineral deposits in the area. The relatively low eTh concentration matches other geological units (Figure 9b). The high concentration of equivalent uranium (eU) within the range of 4.32 ppm – 5.22 ppm predominates in major amphibolite and granitoid rocks and trends eastward toward the south region. In comparison, the low level of uranium eU concentration below 0.66 ppm verifies the major water body (Figure 9c).

3.3.2 eTh/K Ratio map

The eTh/K ratio in the radiometric data was instrumental in distinguishing the three major lithotype units (A, B, and C) and in recognizing zones affected by hydrothermal alteration (Figure 10a). The lithotype unit A is characterized by high eTh/K ratios, indicating a high thorium-to-potassium ratio. Since thorium remains immobile during alteration, while potassium is considered easily mobilized, these high ratios indicate relatively unaltered, compositionally mature lithologies such as stable sedimentary or metasedimentary rocks. The lithological unit B displays moderate, more variable eTh/K values, suggesting a mixture of sedimentary units with differing mineralogical

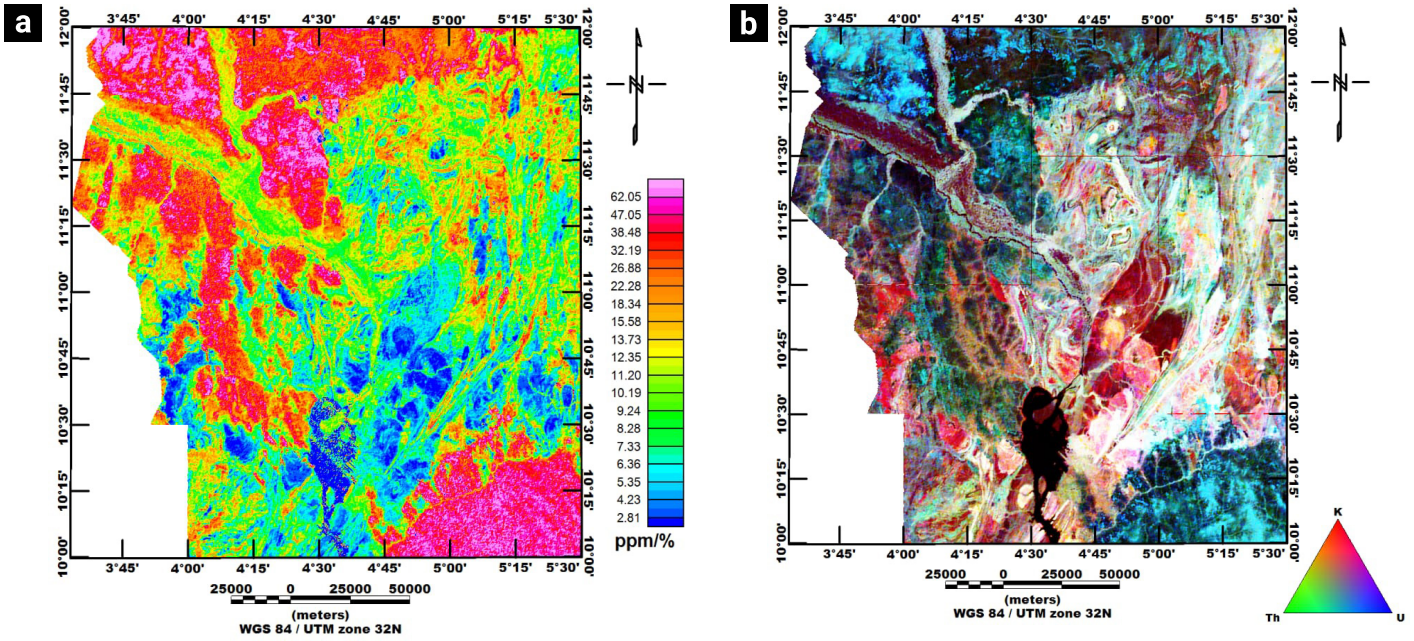


Figure 10. (a) Ratio of eTh/K map with designated lithological zones A-C, (b) Ternary map.

compositions, including feldspar-bearing layers that contribute to elevated potassium. This intermediate signature produces a gradational boundary between lithotype units A and B (Figure 10a). The most distinctive patterns occur in lithotype unit C, where consistently low eTh/K ratios highlight zones enriched in potassium relative to thorium. These low-ratio anomalies are characteristic of hydrothermal alteration, particularly processes that introduce or redistribute potassium through sericitization, illitization, or K-feldspar alteration. Consequently, the sharp transition from moderate or high eTh/K values in lithotype units A and B to low ratios in lithotype unit C defines a clear lithological boundary while simultaneously marking potential alteration zones. The spatial clustering of these low eTh/K anomalies within and around lithotype unit C also suggests structurally controlled fluid movement, further supporting their interpretation as hydrothermally modified areas.

The ternary eTh, eU, K map (Figure 10b) provides a complementary and visually intuitive way to distinguish the three lithotype units (A, B, and C) and to highlight areas affected by hydrothermal alteration. In this image, the colors represent the relative proportions of thorium (eTh), uranium (eU), and potassium (K), allowing each unit to be identified by its dominant radioelement signature. Lithotype unit A appears in colors that trend toward the eTh rich corner, indicating rocks with high thorium relative to potassium and uranium. This geochemical character is typical of relatively unaltered, mature sedimentary or metasedimentary units in which eTh bearing minerals remain stable. Lithotype unit B shows mixed hues positioned between the eTh and K components, reflecting intermediate proportions of these elements. This variability corresponds to heterogeneous sedimentary successions containing mixtures of feldspar, clay minerals, and detrital heavy minerals(Figure 10b. The lithotype unit C stands out clearly in K dominant colors, particularly where bright potassium-rich tones appear along structural zones. These intense K signatures are characteristic of potassium enrichment associated with hydrothermal processes such as sericitization or K-feldspar alteration (Figure 10b).

When compared with the eTh/K ratio map (Figure 10a), the ternary representation reinforces the same spatial patterns. Areas mapped as low eTh/K ratios map (Figure 10b), interpreted as hydrothermally altered zones correspond precisely to the K rich domains in the ternary map, confirming the influence of K metasomatism. Similarly, regions with high eTh/K values align with eTh-dominant colors in the ternary image, indicating more stable, unaltered lithologies. Thus, the ternary map not only distinguishes lithotype units A, B, and C based on their radioelement signatures but also verifies the alteration patterns inferred from the ratio map, providing a consistent and integrated geochemical interpretation of the terrain

4. Conclusion

The high-resolution airborne geophysical datasets of the southwestern part of Sokoto basin, Northwestern Nigeria, were interpreted to delineate lithological units, magnetic sources, and geometry (lateral and vertical extent) of the geologic features. The Landsat8 airborne data enhanced images as RGB band

753, depicting the dominant lithologic units corresponding to metamorphic rocks within the E-S region, in contrast, the older granitoids in the SW region and the major water body and alluvium traverse in NW orientation. However, the lithological associations contained in VNIR and SWIR bands pass information that is attributable to Fe-oxides, carbonates, and clays' occurrence. The RTE–RMA produced low magnetic responses within the sedimentary domain and relatively high magnetic responses within the metamorphic rock. The analytic signal and tilt derivative anomalies unveil the edges (transition zones) of the established metamorphic, sedimentary rocks, and metasedimentary. The distribution of radioelement's potassium, thorium, and uranium, aid in distinctly classifying the lateral lithologies mapped with the enhanced Landsat 8 and magnetic anomalies. The vertical extent (magnetic source depths) obtained from the source parameter imaging SPI range from 85 to 754 m which is corroborated with 3D Euler Deconvolution as $\leq$ 200 m, 317.7 to 500 m, and above 780 m, for shallow to intermediate and deeper depths respectively. Euler solution of the structural index of SI= 0; 1 revealed a perfect cluster along notable geologic features. The methods employed in this study have proven to be successful in distinguishing different rock types and improving geological mapping. These techniques can be utilized in a region with contrasting lithological formations, similar to what was observed in this research.

5. Acknowledgements

I would like to thank Abdullahi Fodio University of Science and Technology, Aliero, Nigeria, for the sponsorship support provided through the 2019/2020 Tertiary Education Trust Fund (TETFund) for academic staff. I also appreciate the Nigeria Geological Survey Agency (NGSA) for providing the airborne datasets, the USGS website for the Landsat 8 dataset, and the Department of Physics and Materials Science, Kwara State University (KWASU), Malete, where I completed my Ph.D. Finally, I thank the anonymous reviewers for their valuable comments and contributions, which significantly improved this manuscript.

6. References

Adeleye, D. R. (1979). A review of Mastrichian paleogeography of the Southern Illummeden and Nupe Basin. Journal of mineral and geology, 16(2), 119-123.

Ademila, O., Akingboye, A. S. & Ojamomi, A. I. (2018). Radiometric survey in geologic mapping of parts of the basement complex area of Nigeria. Vietnam Journal of Earth Sciences 40(3), 288–298. doi: **https://doi.org/10.15625/0866-7187/40/3/12619**

Ahmed, A. (2020). Hydrothermal alteration mapping for geothermal alteration in Manda-INakir Area, NW of the Republic of Djibouti. Proceedings World Geothermal Congress, Reykjavik, Ireland.

Airo, M. L. & Mertanen, S. (2008). Magnetic signatures related to orogenic gold mineralization, Central Lapland Greenstone Belt, Finland. Journal of Applied Geophysics, 64(1), 14–24. doi: **https://doi.org/10.1016/j.jappgeo.2007.10.003**

Aisabokhae, J. E., Osazuwa, I. B. (2021). Radiometric mapping and spectral-based classification of Rocks using remote sensing data analysis: the Precambrian Basement complex, NW Nigeria. Remote Sensing Applications: Society and Environment, 21, 100447. doi: **https://doi.org/doi:10.1016/j.rsase.2020.100447**

Akingboye, A. S., Ademila, O., Ogunyele, A. C. (2018). Improved magnetic data analyses and enhancement techniques for lithological and structural mapping around Akure, Southwestern Nigeria. Earth Sciences Malaysia 2(1), 16–21. doi: **https://doi.org/10.26480/esmy.01.2018.16.21**

Akinlalu, A. A., Adelusi, A. O., Olayanju, G. M., Adiat, K. A. N., Omosuyi, G. O., Anifowose, A. Y. B., Akeredolu, B. E. (2018). Aeromagnetic mapping of basement structures and mineralization characterization of Ilesa Schist Belt, Southwestern Nigeria. Journal of African Earth Sciences, 138, 383–391. doi: **https://doi.org/10.1016/j.jafrearsci.2017.11.033**

Akinsunmade, A., Nguyen Dinh, C., Wojas, A., Tomecka-Suchon, S. (2020). Characterization of lithological zones of the Isanlu sheet 225, North Central Nigeria, using aero-geophysical datasets. Acta Geophysics. 68, 651–665. doi: **https://doi.org/10.1007/s11600-020-00411-6**

Ali, A., Pour, A. B. (2014). Lithological mapping and hydrothermal alteration using Landsat 8 data: A case study in the Arab mining district, Red Sea Hills, Sudan. International Journal of Basic and Applied Sciences. 3(3), 199–208. doi: **https://doi.org/10.14419/ijbas.v3i3.2821**

Allou, G., Bonin, B. (2015). "The Landsat7 ETM+ remote sensing imagery for lithological and Structural mapping in Cote d'ivoire (West Africa): Case of Dabakala area. European Scientific Journal, 11(36), 141–163. doi: **https://doi.org/10.19044/esj.2015.v11n36p%25p**

Amara, B. N., Aissa, D. E., Maouche, S., Guessoum, N. (2019). Hydrothermal alteration Mapping and structural features in the Guelma basin (Northeastern Algeria): contribution of Landsat-8 data. Arabian Journal of Geosciences, 12, 19–27. doi: **https://doi.org/10.1007/s12517-019-4224-4**

Augie, A. I, Magawata, Y. I., Saleh, A., Magawata, U. Z., Garba, N. (2022). Tracing the structure Associated with manganese over the western part of Kebbi using Aeromagnetic data. Journal of Pure and Applied Sciences, 22, 28-34. doi: **http://dx.doi.org/10.5455/sf.augie22**

Bruno, V., Derk, F., Chris, M. G., Chris, M. (2004). New insights into Magnetic derivatives for structural mapping. The Leading Edge, *23(2)*, 116–119. doi: **https://doi.org/10.1190/1.1651454**

Dentith, M., & Mudge, S. T. (2014). *Geophysics for the mineral exploration geoscientist*. Cambridge University Press.

Deroin, J. P. (2019). An overview of 40 years of remote sensing geology based on Arab examples. In. Bendaoud, A., Hamimi, Z., Hamoudi, M., Djemai, S., Zoheir, B. (Eds) The Geology of the Arab World (pp. 427-453). Springer Geology. doi: **https://doi.org/10.1007/978-3-319-96794-3_12**

Ekwok, S. E., Akpan, A. E., Achadu, O. M., Eze, O. E. (2021). Structural and lithological interpretation of aero-geophysical data in parts of the Lower Benue Trough and Obudu Plateau, Southeast Nigeria. Advances in Space Research, 68(7), 2841-2854. doi: **https://doi.org/10.1016/j.asr.2021.05.019**

Emmanuel, E. O., Justus, O. I., Chuka, J. O. (2020). Near-surface Characterization of sediments of the Sokoto group exposed around Wamakko area, Northwestern Nigeria: an integrated approach. Geology, Ecology, and Landscapes, 5(2), 81-93. doi: **https://doi.org/10.1080/24749508.2020.1833628**

Emujakporue, G., Ofoha, C. C. & Kiani, I. (2018). Investigation into the basement morphology and tectonic lineament using aeromagnetic anomalies of Parts of Sokoto Basin, North Western, Nigeria. Egyptian Journal of Petroleum, 27(4), 671–681. doi: **https://doi.org/10.1016/j.ejpe.2017.10.003**

Evans, D. (1988). Multi-sensor classification of sedimentary rocks. Remote Sensing of Environment, 25(2), 129–144. doi: **https://doi.org/10.1016/0034-4257(88)90097-1**

Fagbohun, B. J., Oluseyi, A. B., Femi., J. A., Ayotunde, A. O., Blessing, A. (2021). Identifying geochemical anomalies and spatial Distribution of gold and associated elements in the Zuru Schist Belt, northwest Nigeria. Arabian Journal of Geosciences, 14(508). doi: **https://doi.org/10.1007/s12517-021-06828-7**

Fitches, W. R., Ajibade, A. C., Egbuniwe, I. G., Holt, R. W., & Wright, J. B. (1985). Late Proterozoic schist belts and plutonism in NW Nigeria. *Journal of the Geological Society*, *142*(2), 319-337.

Farah, A., Ahmed, A. Abdellah, A., Mohamed, A. & Mohammed, I. (2021). Lithological mapping using Landsat 8 OLI multispectral data in Boumalne, Imider, and Sidi Ali Oubork, High Central Atlas, Morocco. E3S Web of Conferences, 234, 17. doi: **https://doi.org/10.1051/e3sconf/202123400017**

Garba, I. (2000). Origin of Pan-African mesothermal gold mineralization at Bin Yauri, Nigeria. Journal of African Earth Sciences, 31(2), 433–449. doi: **https://doi.org/10.1016/S0899-5362(00)00098-1**

Garba, I. (2003). Geochemical characteristics of mesothermal gold mineralisation in the Pan-African (600 ± 150 Ma) basement of Nigeria. Applied Earth Science, 112(3), 319–326. doi: **https://doi.org/10.1179/0371745032250031**

Ghrefat, H., Ali, Y., Kahal. A.,Hussain J., Alfaifi, S. (2021). Utilization of multispectral Landsat8 remote sensing data for lithological mapping of southwestern Saudi Arabia. Journal of King Saud University of Science, 33, 101414. doi: **https://doi.org/10.1016/j.jksus.2021.101414**

Kogbe, C. A. (1979). Geology of the south eastern (Sokoto) sector of the Iullemmeden Basin. Department of Geology, Ahmadu Bello University.

Kogbe, C. A. (1981). Cretaceous and tertiary of the Iullemmeden Basin in Nigeria (West Africa). Cretaceous Research, 2(2), 129-186. doi: **https://doi.org/10.1016/0195-6671(81)90007-0**

Li, Y., Oldenburg, D.W. (1996). 3-D inversion of magnetic data: Geophysics, 61, 394–408.

MacLeod, I. N., Jones, K., & Dai, T. F. (1993). 3-D analytic signal in the interpretation of total magnetic field data at low magnetic latitudes. *Exploration geophysics*, *24*(4), 679-688.

Magawata, U. Z., Olasunkanmi, N. K., and Issa, T. A. (2024). Geothermal parameter assessment in the Southwestern Sokoto Basin, Nigeria, using spectral analysis (centroid method). Recent Advances in Natural Sciences, 2(1), 47-47. doi: **https://doi.org/10.61298/rans.2024.2.1.47**

Magawata, U. Z., Olasunkanmi, N. K., Egbeyale, G. B., and Saleh, A. (2025). Structure and mineralization potential of the southwestern part of Sokoto Basin in Nigeria. Frontiers in Earth Science, 13. doi: **https://doi.org/10.3389/feart.2025.1500162**

Nabighian, M. N. (1972). The analytic signal of two-dimensional magnetic bodies with Polygonal Cross-section: its properties and us for automated anomaly interpretation. Geophysics, 37(3), 507-517. doi: **https://doi.org/10.1190/1.1440276**

Nigerian Geological Survey Agency. (2009). Airborne Geophysical Survey total magnetic Intensity map and Radiometric Map of the Southern part of Sokoto basin (16 Sheets).

Nwajide, C. S. (2013). Geology of Nigeria's Sedimentary Basins. CSS Bookshops Limited, Lagos.

Obaje N.G. (2013). Updates on the geology and mineral resources of Nigeria. Onaivi Printing & Publishing.

Obaje, N. G. (2009). Geology and mineral resources of Nigeria. Springer. doi: **https://doi.org/10.1007/978-3-540-92685-6**

Offodile, M. E. (2002). *Ground water study and development in Nigeria*. Mecon Geology & Eng. Services.

Okon, E. E., Ikeh, J. O., & Offodile, C. J. (2020). Near-surface characterization of sediments of the Sokoto group exposed around Wamakko area, Northwestern Nigeria: an integrated approach. *Geology, Ecology, and Landscapes*, *5*(2), 81-93.

Okpoli, C. C., Akingboye, A. S. (2019). Application of high-resolution gravity data for litho-structural and depth characterization around the Igabi area. Northwestern Nigeria- NRIAG Journal of Astronomy and Geophysics 8 (1), 231–241. doi: **https://doi.org/10.1080/20909977.2019.1689629**

Olasunakanmi, N.K., Magawata, U.Z., Bayowa, O.G. (2023). Assessment of image ratio technique: targeting structural features and mineralization characteristics in the southwestern part of the Sokoto Basin in Nigeria using Landsat 8 imagery, Kuwait Journal of Science, 50(4), 803-811. doi: **https://doi.org/10.1016/j.kjs.2023.02.030**

Olatunji, S. (2022). Integration of remote sensing and geophysical methods for structural and litho-logical mapping in a part of Precambrian basement rocks, northern Nigeria. Journal of Fundamental and Applied Sciences, 14(1), 161-180. doi: **https://doi.org/10.4314/jfas.v14i1.9**

Olsunkanmi, N.K., Olufemi, O.A., Olatunji, S. Salawa, N.B., Toba, B. (2020). Interpretation of High-resolution aeromagnetic data of Kaoje and its environment, the western part of the Zuru Schist belt, Nigeria: implication for Fe–Mn occurrence. Heliyon, 6(1). doi: **https://doi.org/10.1016/j.heliyon.2020.e03320**

Pour, A.B., Hashim, M. (2015). Hydrothermal alteration mapping using Landsat-8 data, Sar Cheshmeh copper mining district, SE Iran. Journal of Taibah University for Science, 9(2), 155-166. doi: **https://doi.org/10.1016/j.jtusci.2014.11.008**

Rajagopalan, S. (2003). Analytical signal vs reduction to pole: solutions for low magnetic Latitude Exploration Geophysics, 34(4), 257–262. doi: **https://doi.org/10.1071/EG03257**

Ramadan, T. M., Abdel Fattah, M. F. (2010). Characteristics of gold mineralization in Garin Hawal area, Kebbi State, NW Nigeria, using remote sensing. The Egyptian Journal of Remote Sensing and Space Science, 13(2), 153–163. doi: **https://doi.org/10.1016/j.ejrs.2009.08.001**

Ranjbar, H., Masoumi, F., Carranza., E. J. M. (2011). Evaluation of geophysics and space Borne multispectral data for alteration mapping in the SarCheshmeh mining area, Iran. International Journal of Remote Sensing, 32(12), 3309–3327. doi: **https://doi.org/10.1080/01431161003745665**

Raoufou, D., GNAMMI, Y., Gérard, A., d'ALMEIDA, K., Christophe, K., Nicaise, Y. (2016). Use of Landsat 8 OLI and Aeromagnetic Data for Structural Mapping of Pako Basin Region, North Benin. *Journal of Geosciences and Geomatics*, 8(2), 45-57.

Reid, A. B., Allsop, J. M., Granser, H., Millett, A. J., Somerton, I. W. (1990). Magnetic interpretation in three dimensions using Euler deconvolution. Geophysics. 55(1), 80–91. doi: **https://doi.org/10.1190/1.1442774**

Roest, W. R., Verhoef, V., Pilkington, M. (1992). Magnetic interpretation using the 3-Danalytic Signal. Geophysics, 57(1), 116–125. doi: **https://doi.org/10.1190/1.1443174**

Sabins, F. F. (1987). Remote sensing principles and interpretation. W. H. Freeman, New York, NY.

Sabins, F. F. (1997). Remote Sensing: principles and interpretation (13 ed.). W. H. Freeman, New York, NY.

Saleh, A., Qudus, B., Magawata, U. Z. & Augie, A. I. (2020). Delineation of structural features and Depth to the magnetic sources over Allawa and its environs North-central Nigeria. International Journal of Advances in Engineering and Management, 2(6), 545-553, doi: **https://doi.org/10.35629/5252-0206545553**

Salem, A., Williams, S., Fairhead, J. D. E., Ravat, D., Smith, R. (2007). Tilt-depth method: A simple depth estimation method using first-order magnetic derivatives. *The Leading Edge*, *26*(12), 1502–1505. doi: **https://doi.org/10.1190/1.2821934**

TakodjouWambo, J. D., Pour, A. B., Ganno, S., Asimow, P. D.,Zoheir, B., Salles, R. D. R. Nzenti, J. P. Pradhan, B. & Muslim, A. M. (2020). Identifying high-potential zones of gold Mineralization in a sub-tropical region using Landsat 8 and ASTER remote sensing data: A case study of the Ngoura-Colomines gold field, eastern Cameroon. Ore Geology Reviews, 122, 103530. doi: **https://doi.org/10.1016/j.oregeorev.2020.103530**

Thurston, J. B., Smith, R. S. (1997). Automatic conversion of magnetic data to depth, dip, and susceptibility contrast using the SPI ™ method. Geophysics, 62(3), 807-813. doi: **https://doi.org/10.1190/1.1444190**

Traore, M., TakodjouWambo, J. D., Ndepete, C. P., Tekin, S., Pour, A. B. & Muslim, A. M. (2020). Lithological and alteration mineral mapping for alluvial gold exploration in the South East of the Birao area, Central African Republic using Landsat-8 Operational Land Imager (OLI) data. Journal of African Earth Sciences. 170, 103933. doi: **https://doi.org/10.1016/j.jafrearsci.2020.103933**

U.S. Geological Survey. (2021). *Geophysical data and analysis*. **https://www.usgs.gov**

Verduzco, B., Fairhead, J. D., Green, C. M., Mackenzie, C. (2004). New insights into magnetic derivatives for structural mapping. *The Leading Edge,23(2)*, 116–l19. Doi: **https://doi.org/10.1190/1.1651454**

Wang, J. & Meng, X. (2019). An aeromagnetic investigation of the Dapai deposit in Fujian Province, South China: Structural and mining implications. Ore Geology Reviews, 112. doi: **https://doi.org/10.1016/j.oregeorev.2019.103061**

Waswa, A. K., Nyamai, C. M., Mathu, M. M., Ichangi, D. W. (2015). Integration of geological mapping and remotely sensed studies for the discovery of iron ore mineralization Inmutomo-Ikutha Area, SE Kenya. Universal Journal of Geosciences 3(2), 39–50. doi: **https://doi.org/10.13189/ujg.2015.030201**

Wright, J. B., Hastings, D. A., William, H. R. (1985). Geology and Mineral Resources of West Africa. Springer Dordrecht. doi: https://doi.org/10.1007/978-94-015-3932-6